

Formation of the Ionospheric G-condition Following the 2017 Great American Eclipse

S. Chakraborty¹, L. Qian², S. Mrak³, J. M. McInerney², J. Mabie⁴, G. Earle¹,
L. Goncharenko⁵, and P. J. Erickson⁵

¹Center for Space Science and Engineering Research, Virginia Tech, Blacksburg, VA

²High Altitude Observatory, National Center for Atmospheric Research, Boulder, CO

³Space Weather Technology, Research and Education Center, University of Colorado Boulder, Boulder,
CO

⁴National Centers for Environmental Information, NOAA, Boulder, CO

⁵Haystack Observatory, Massachusetts Institute of Technology, Westford, MA

Key Points:

- Solar eclipses cause altitude-dependent ionospheric plasma density depletion and recovery effects attributed to changing ion composition
- The recovery time-scale varies with altitude, causing a phase where $NmF_1 \geq NmF_2$
- The G-condition is caused by slower recombination in the O^+ dominated F_2 -layer compared to faster recovery at lower altitudes

Corresponding author: Shibaji Chakraborty, shibaji7@vt.edu

Abstract

A total solar eclipse (TSE) crossed the continental US (CONUS) from west to east on 21 August 2017. Ionosondes located under the eclipse totality at Lusk (Wyoming) and Boulder (Colorado) observed the ionospheric G-condition 20 minutes after totality. The Millstone Hill mid-latitude incoherent scatter radar recorded an anomalous low altitude F_2 peak during the recovery phase of the eclipse, which can be attributed to an ionospheric G-condition. We perform WACCM-X simulations to investigate the physical processes that drive the ionospheric G-condition. Specifically, we conduct a diagnostic analysis of the simulated atomic oxygen ion continuity equation to examine the source of the G-condition. Results indicate that (a) perturbations in plasma density of E and F_1 -layers closely follow the TSE occultation, whereas the F_2 -layer density depletion lags the occultation by 20-minutes; (b) this delay increases with altitude and is caused by slower ion recombination in the diffusion-dominated F_2 -layer; (c) the delay creates a time period during eclipse recovery when plasma density of the F_1 -layer is larger than that of the F_2 -layer, which manifests as the G-condition. The simulation study showed an increase in the strength of the ionospheric G-condition with latitude, which disagrees with previously reported studies.

Plain Language Summary

Solar radiation is the primary source of the ionosphere. The eclipse-driven sudden disappearance of solar irradiance provides an opportunity to study how the ionosphere behaves under this controlled environment. Ground-based observations during the 21 August 2017 Great American Eclipse (GAE) provide evidence of the existence of an ionospheric G-condition, where the plasma density of the ionospheric F_1 -layer exceeds that of the F_2 -layer. This paper provides the first explanation of the formation mechanism of the ionospheric G-condition following a total solar eclipse. We use simulations from a physics-based model to infer the physics behind the ionospheric G-condition. The combination of observations and model predictions provides insight into the formation mechanism of these unusual conditions following the 2017 GAE.

1 Introduction

A total solar eclipse (TSE) provides a unique opportunity to study ionospheric plasma dynamics and various other types of geophysical phenomena under a “controlled” environment. Among various geophysical events that can be probed during a TSE, the ionospheric G-condition is relatively unexplored. The ionospheric G-condition occurs when the peak plasma density associated with the F_1 -layer, which is composed of molecular ions (M^+ : NO^+ , N_2^+ , and O_2^+), becomes larger than or equal to that of the F_2 -layer, which is mainly composed of atomic ions (O^+), i.e., $NmF_1 \geq NmF_2$ (Rishbeth & Garriott, 1969; Lobzin & Pavlov, 2002; Deminov et al., 2011; Buonsanto, 1990; Cummack, 1961). Observational studies using ionosonde and incoherent scatter radar (ISR) measurements reported that the occurrence probability of the G-condition increases with geomagnetic activity, latitude, and decreasing solar zenith angle and solar activity (Oliver, 1990; Fukao et al., 1991; Banks et al., 1974; Häggström & Collis, 1990). Additionally, numerical studies suggested that the escape of atomic oxygen ions and associated electrons (O^+/e^-) from the F_2 -layer keeps the F_1 -layer relatively unperturbed during the above-mentioned geophysical conditions, creating the flip ($NmF_1 \geq NmF_2$) in the density profile that leads to the G-condition (Deminov et al., 2011). A study by Rishbeth (1968) mentioned these phenomena occurring following a solar eclipse and mentioned an eclipse-driven $F_{1\frac{1}{2}}$ -layer, which is predominately observed in low magnetic latitudes. Rishbeth (1968) suggested that altitude dependent recombination rate is the primary driver of this phenomena. The sources of the ionospheric G-condition have been previously studied using observations

and numerical modeling (A. V. Pavlov & Buonsanto, 1998; A. Pavlov et al., 1999; Schlessier & Buonsanto, 1999; Deminov et al., 2011).

Bullett and Mabie (2018) reported the ionospheric G-condition following the 2017 Great American Eclipse (GAE) in vertical and oblique ionosonde observations. The investigation suggested that the responses of the E and F₁-layers are primarily driven by the photochemical processes that are modified by the obscuration of the solar disk via the moon’s shadow (Chen et al., 2011; Zhang et al., 2017). In addition, the study suggested the response of the F₂-layer is dominated by transport phenomena. Goncharenko et al. (2018) also reported a very low (below 200 kilometers) F₂-layer peak height following the GAE over the mid-latitude Millstone Hill observatory using incoherent scatter radar data. However, no previous study has pointed out the ionospheric process that manifests the ionospheric G-condition following a TSE using first principles-based physical modeling. While the primary loss mechanism that governs photochemical reactions and changes in plasma density can be explained through simple occultation of solar radiation, a comprehensive explanation of eclipse-associated physical processes is more complex, since it must include effects of altered ionospheric-thermospheric (IT) coupling and related space weather effects (Chen et al., 2015). Rishbeth (1968), mentioned that the strength of a TSE-driven ionospheric G-condition becomes lower with the increase in latitude. It is hypothesized that at higher latitudes plasma diffusion from the conjugate hemisphere along the field line fills the TSE-induced plasma vacancy at the F₂-layer altitude which reduces the occurrence probability of the ionospheric G-condition. However, no previous study has confirmed this predicted latitudinal variance of G-condition using both observations and model validations.

In this article, we report the results of a simulation study using the Whole Atmosphere Community Climate Model with a Thermosphere and Ionosphere eXtension (WACCM-X) to investigate the formation processes of the ionospheric G-condition following the 2017 GAE. In addition, we validate the following postulate by (Rishbeth, 1968): ‘eclipse F₁₂-layer is predominately observed in low magnetic latitudes’. We perform a diagnostic analysis of the model outputs and directly compare them with Millstone Hill ISR data and ionosonde observations to understand the IT coupling processes that manifest the ionospheric G-condition. In the following sections, we describe the dataset, model used, and the results obtained from the study. Finally, we discuss the phenomena and their sources and conclude our findings. Major findings of this study are: (a) the depletion in F₂-layer density lags the eclipse totality by at least 20 minutes, (b) the effect increases with altitude, and (c) this delay during eclipse recovery creates a time period when foF₁ is larger than foF₂, causing a G-condition that lasted about 50 minutes.

2 Datasets & Model

In this section we describe the datasets and the model used in this study. Figure 1 presents the locations of different instruments used in this study, across CONUS. The eclipse obscuration shadow (occultation, α) during the peak of eclipse totality is overlaid and color-coded by the color bar on the right. The region enclosed by red and black dotted curves indicates the location of eclipse totality during the TSE passage. The location of the ionosonde is color-coded in blue, while the mid-latitude incoherent scatter radar located at Millstone Hill is color-coded in red.

2.1 Ionosonde

During this eclipse, Bullett and Mabie (2018) conducted a vertical and oblique HF sounding experiment between a permanent ionosonde station at Boulder, CO (39.992°N 105.269° W) and a VIPIR instrument from the U.S. Naval Research Laboratory at a temporary field site within the ground path of totality in Lusk, WY (42.750° N, 104.455° W). This HF communication geometry provides a great circle distance of 313 kilome-

ters with a bearing angle of 12° W, which is nearly parallel to the geomagnetic field lines with a declination angle of 8° . Due to this geometry, Near Vertical Incidence Skywave (NVIS) propagation at Lusk was outside of totality whereas the same at Boulder was near totality. Effects of the G-condition can be seen in the oblique and NVIS propagation observed by both ionosondes.

Figure 2(a-b) present observations from the ionosondes located at Lusk (WY) and Boulder (CO) showing the ionospheric G-condition in the vertical sounding experiment reported by Bullett and Mabie (2018). It shows observed plasma frequency at F_1 (~ 150 kilometers altitude, foF_1) and F_2 (~ 240 kilometers altitude, foF_2) peaks along with the occultation function (in black). The peak foF_2 density reduction lags about 20 minutes behind the peak in foF_1 reduction, which follows the eclipse occultation at both altitudes. For reference, the maximum occultation is identified by a black vertical line at 17:46 UT. Note that the ionosondes stop observing bottomside vertical sounding echoes from 240 kilometers soon after maximum occultation at both locations, suggesting a $foF_1 \geq foF_2$ condition.

2.2 Incoherent Scatter Radar (ISR)

The Millstone Hill ISR (MHISR: 42.6° N, -71.5° W) uses the radar technique of collective Thomson backscatter to provide ionospheric plasma parameters as a function of altitude. MHISR was operational for five consecutive days starting on 19 August 2017. During this eclipse, MHISR was located more than 1,000 kilometers northeast from the center of totality; its maximum obscuration level was $\sim 63\%$. Goncharenko et al. (2018) reported several features of eclipse response observed at mid-latitudes using MHISR observations. In this study, we used the electron density (N_e) profiles available from the CEDAR Madrigal database. Electron density profiles from the radar observations extend from 90 kilometers to ~ 600 kilometers, but this study focuses on the 100-300 km altitude range. This enables us to analyze photochemical reactions and transport processes that drive the G-condition. MHISR data provide direct observational evidence of the G-condition in the ionosphere following the 2017 GAE. Figure 2(c), adapted from Goncharenko et al. (2018), presents the temporal evolution of the electron density observed using MHISR. We observed a general drop in electron density following the TSE. However, electron density recovery after the time of maximum eclipse penumbral obscuration (indicated by a central vertical dotted line) was not symmetrical across the altitudes. In particular, we observed a relative delay in the recovery of electron densities at altitudes greater than 200 kilometers following maximum obscuration. This delay created a differential altitude response in mid-latitude ionospheric parameters at Millstone Hill. In particular, the delay in the differential response increased with height.

2.3 Eclipse Occultation: pyEclipse

To examine the TSE-driven effects on the ionosphere-thermosphere system, we modified the solar irradiance with the eclipse occultation mask using the pyEclipse model (Mrak et al., 2022). We computed the uniform mask with an inflated solar radius by 12.5% to mimic the source of the Extreme Ultra Violet (EUV) emissions (McInerney et al., 2018), and we use the Solar Dynamics Observatory (SDO) Atmospheric Imaging Assembly (AIA) image of coronal emissions at 17.1 nm for reference in the ionosonde observations. While the SDO AIA mask is important for localized ionospheric density perturbations (Mrak et al., 2018) and satellite observations (Hairston et al., 2018), it does not impact the global morphology of electron density dynamics (i.e., Mrak et al., 2022, Figure 9).

2.4 WACCM-X

The Whole Atmosphere Community Climate Model with thermosphere and ionosphere extension, commonly referred to as WACCM-X, is used to study the sources of

the ionospheric G-condition. WACCM-X has a $1.9^\circ \times 2.5^\circ$ horizontal resolution and a 0.25 scale height vertical resolution above 1 hPa (~ 50 kilometers), with an upper boundary at ~ 600 kilometers, depending on solar activity (Liu et al., 2018, 2010). The thermosphere and ionosphere extension provides a self-consistent thermosphere and ionosphere module that includes calculation of electron, ion, and neutral densities, temperature, self-consistent solution of global electrodynamics including an interactive electric wind dynamo at mid- and low-latitudes, and O^+ transport in the ionospheric F-region. At high latitudes, the electric field of magnetospheric origin is parameterized according to Heelis et al. (1982) or Weimer (2005) or provided by the Assimilative Mapping Ionospheric Electrodynamics procedure (Richmond et al., 1998; Richmond, 1992). Default solar ultraviolet irradiance is parameterized by the F10.7 index or can be supplied by measurements (Solomon & Qian, 2005). To capture solar irradiance variations, WACCM-X uses solar irradiance from the FISM2 (Chamberlin et al., 2020). To examine TSE-driven effects on the ionosphere-thermosphere system, we modified the solar irradiance with the eclipse occultation function. We run the WACCM-X model with and without the eclipse occultation function, to isolate the eclipse effects (McInerney et al., 2018).

The F_1 - and F_2 -layers primarily consist of molecular ions (M^+ : NO^+ , O_2^+ , N_2^+) and atomic oxygen ions (O^+) and associated electrons, respectively. Hence, we analyzed the temporal evolution of molecular ions and electron densities, as well as conducted a diagnostic analysis of the O^+ continuity equation to unveil the formation mechanism of the G-condition. This continuity equation-based diagnostic analysis is described in Lei et al. (2008) and used by Wang et al. (2019). From Rishbeth and Garriott (1969), we can write the F_2 -region's O^+ ion continuity equation as:

$$\frac{\partial [O^+]}{\partial t} = p - l - \nabla \cdot ([O^+] \vec{V}) \quad (1)$$

where, $[O^+]$, p , l , and $-\nabla \cdot ([O^+] \vec{V})$ are the density of O^+ ion, rate of photoionization, loss due to the chemical recombination process, and plasma transport due to various ionospheric processes, respectively. These ionospheric processes are electric fields ($D_{\vec{E} \times \vec{B}}$), neutral wind (D_{wind}), and ambipolar diffusion (D_α). We can rewrite equation (1) as:

$$\frac{\partial [O^+]}{\partial t} = p - l + D_{\vec{E} \times \vec{B}} + D_{\text{wind}} + D_\alpha \quad (2)$$

Our study is primarily focused on physical processes around 150 kilometers and 240 kilometers. We use the differential difference (δ) defined in equation (3) to analyze the outputs from the WACCM-X model.

$$\delta^\tau(\mu) = (\mu_{\text{eclipse}}^\tau - \mu_{\text{eclipse}}^{\tau-1}) - (\mu_{\text{non-eclipse}}^\tau - \mu_{\text{non-eclipse}}^{\tau-1}) \quad (3)$$

Consequently, the differential-difference (δ) operator describes temporal changes in any parameter (μ) obtained from the WACCM-X run. The subtraction of the temporal variations of the non-eclipse run from the temporal variations of the eclipse run effectively removes the local time variations from the variations due to the eclipse. In addition, we compare the temporal evolution of the simulated molecular ions and atomic oxygen ion densities to contrast the eclipse effects in the F_1 - and F_2 -layers.

2.4.1 Defining the strength of the ionospheric G-condition

It is useful to define metrics gauging the strength of the G-condition, as these can be important in the quantification of eclipse-driven effects on the trans-ionospheric HF propagation and IT system. To quantify the ionospheric G-condition we introduce the following parameters: (i) duration of the G-condition (ΔT_{GC}), and (ii) maximum change in NmF_1 – NmF_2 during the G-condition (GC^p). Note that ground-based HF sounders, such as ionosondes, can only map the bottom side ionosphere; hence, they observe only the F_1 -peak because $foF_1 \geq foF_2$ during the G-condition. For these reasons metric (ii) defined above would not be applicable to these observations.

3 Simulation Results

From observations and models, we find a general decrease in electron density after the eclipse over Lusk (WY), Boulder (CO), and Millstone Hill (MA) (Figure 2). During the eclipse, we observed a decrease in electron density at different altitudes of the ionosphere. However, the peak depletion and recovery of the electrons at the F₂-layer were delayed relative to the temporal variations of the eclipse occultation.

3.1 Data-model Comparison over Lusk (WY)

The outputs of the model and data-model comparison over Lusk, WY are presented in Figure 3 to show the agreement between observations recorded by ionosondes and WACCM-X model simulation. The figure shows modeled plasma frequency at F₁ (~150 kilometers altitude, foF₁) and F₂ (~240 kilometers altitude, foF₂). Panels (a) and (b) present observations from the ionosonde located over Lusk (WY), and WACCM-X simulated foF_{1,2} over Lusk (WY). From the observation presented in panel (a) we find the ionospheric G-condition lasted about 50 minutes during the recovery phase of the eclipse. As a consequence of the ionospheric G-condition we observed an asymmetrical eclipse response in the ionosphere as shown in MHISR observations (refer to Figure 2(c)) and mentioned in previous studies (Wang et al., 2019; Goncharenko et al., 2018). The simulation results are presented in panel (b). We find the duration of the modeled G-condition (ΔT_{GC}) and maximum change in NmF₁–NmF₂ are 50 minutes and 76.5 el/cm⁻³, respectively. Furthermore, we observe a 20-minute delay in peak foF₂ response with respect to the eclipse peak occultation (identified by a black vertical line at 17:46 UT) in both data and simulation results, which is also consistent with the Global Ionosphere Thermosphere Model results at the same area (Mrak et al., 2022). In aggregate, these results confirm that the TSE-driven ionospheric conditions that are relevant to the G-condition are well reproduced in the simulated plasma density.

3.2 Simulation Result Analysis

To demonstrate the delay in peak depletion, recovery phase, and the altitudinally differential behavior observed in both ionosonde and ISR observations, we present the electron, molecular ion M⁺, and diagnostic terms of the O⁺ continuity equations, in differential-difference format (equation (3)). Figure 4 presents the 2D time-altitude distribution of WACCM-X simulated electron and M⁺ densities over Lusk (WY). Panels (a) and (b) present electron and M⁺ density to show the difference in their response time with respect to the eclipse timings, respectively. The vertical magenta curves in panels (a) and (b) indicate the time when the parameter (electron or M⁺ density) reaches its minimum value, as a function of altitude. Note that charge neutrality is a good assumption in the ionosphere. Molecular ions dominate in the E- and F₁-regions, whereas O⁺ dominates in the F₂-layer. Therefore, the electron density is roughly equal to the sum of the molecular ion number density in the E- and F₁-regions, and electron density and O⁺ density are roughly equal in the F₂-region. Note that M⁺, which represents the F₁-layer, responds to the eclipse occultation function, and does not show a delay in its response. In contrast, the peak depletion in electron density at the F₂-heights (≥ 190 kilometers) shows a delay of a few minutes to an hour. The longer delays occur at higher altitudes during the eclipse recovery phase. Wang et al. (2019) mentioned a similar time delay and asymmetrical behavior in F₂-layer response in their modeling study. According to a data-based study by Tsai and Liu (1999) and Zhang et al. (2017), major depressions in TEC data are delayed by a few tens of minutes with respect to eclipse totality.

Next, we analyze different terms from the O⁺ continuity equation. Figure 5 presents diagnostic terms associated with photochemical (a) production, (b) loss, (c) production-loss, transport due to (d) neutral wind, (e) ambipolar diffusion, and (f) $\vec{E} \times \vec{B}$ drift processes from the O⁺ continuity equation. Note, that the production process follows the

eclipse occultation function, whereas the loss processes show a delay with respect to the maximum eclipse. Note that panels represent the instantaneous second derivative of O^+ change due to each term in the O^+ continuity equation, while the actual rate of O^+ density change due to each term at any time is the accumulated (integrated) second derivative of O^+ changes up to that time. If we compare the rate of O^+ changes at lower and higher altitudes in panel 5(c), which is the rate of O^+ change due to the sum of photochemical production and loss, then the peak depletion at higher altitudes lagged the one at lower altitudes. Panels (d-f) present transport due to neutral wind, ambipolar diffusion, and $\vec{E} \times \vec{B}$ drift. Note that the color bar range of Panels (d-f) is much smaller (± 5) compared to panels 5(c) and 5(a-b), which are $\pm 10 \text{ cm}^{-3}\text{s}^{-1}$ and $\pm 100 \text{ cm}^{-3}\text{s}^{-1}$, respectively. Therefore, we conclude that the production and loss processes play a primary role in observed dynamics compared to plasma transport processes.

Plasma transport due to neutral wind responses before the eclipse reaches over Lusk (WY), because of the regional neutral wind response to thermospheric cooling within the eclipse shadow (Harding et al., 2018; Cnossen et al., 2019).

Ambipolar diffusion then acts to restore changes due to neutral wind transport. In contrast, the $\vec{E} \times \vec{B}$ drift response occurs after the eclipse is overhead at Lusk (WY). This suggests that the change in the electric field following TSE is primarily driven by the redistribution of the ionospheric plasma density. In addition, perturbations in $\vec{E} \times \vec{B}$ drift started with a negative value that shifted towards positive before maximum obscuration and switched to negative afterward. The amplitude in perturbation before the maximum obscuration is much higher than that after the maximum obscuration. These findings suggest that the eclipse-driven \vec{E} -field effect is asymmetrical with respect to maximum obscuration.

To explain the delayed response in the F_2 -layer, in (Figure 6(a-b)) we present the time evolution of the differential difference of the four terms (second derivatives) from the O^+ continuity equation, and the differential difference of electron density (first derivative) time series at 150 (representing the F_1 -layer) and 240 kilometers (representing the F_2 -layer) over Lusk, WY. The time series are color-coded in the figure and the vertical dashed lines show the time of start, maximum obscuration, and end time of the partial eclipse observed at this location. We note the following signatures in the time series, (i) delayed peak O^+ depletion at 240 kilometers compared to the peak eclipse occultation. Note again that, (ii) O^+ changes at any time are the integrated second derivative of O^+ changes up to that time point; and (iii) transport due to neutral wind and ambipolar response before the TSE.

3.3 Mechanism of Formation of the TSE-driven G-condition

The results presented in previous sections are consistent with a dynamic ionospheric response to eclipse conditions as follows. Before the eclipse occurrence, the F_1 -region is in a near photochemical equilibrium state. Consequently, the F_1 -layer electron density remains nearly synchronous (delayed by only a few minutes) with the eclipse occultation, as shown in Figure 6(a-b) and supported by other studies (Goncharenko et al., 2018; Zhang et al., 2017; Wang et al., 2019). From the simulation study presented above, the peak depletion of the F_2 -layer is delayed by 20 minutes, as is the recovery. This delay in the F_2 -layer creates a period when the ion density in the F_1 -layer is recovering while the density in the F_2 -layer is still decreasing (Figure 6(a-b)), and thus, the ion density in the F_1 -layer becomes greater than that in the F_2 -layer, which manifests as the G-condition. The WACCM-X simulation showed that in the F_2 -region, the combined instantaneous eclipse response of the photochemical production and loss processes is much larger than the responses of the plasma transport process, and it is negative up to the point of the peak eclipse occultation. Since in the F_2 -region, the electron density at any instance is the accumulated O^+ change up to that point, the electron density continues to decrease

when the combined effect of the production and loss is negative after the peak eclipse occultation for about 15-20 minutes (the black line in Figure 5(b)). This causes the delay between the peak electron depletion and the peak eclipse occultation.

Up to this point, we have described reasons for an altitude-dependent delayed ionospheric response using the combined effect of photochemical production and loss. A question arises: Why does the combined effect of the photochemical production and loss lag the eclipse occultation? The reason lies in the slower ion recombination rate in the F₂-region, as shown in Figure 5(b). Previously, Richards and Voglozin (2011, refer to Figure 1 and Table 1 for reaction and recombination rate coefficients) reported the recombination rate coefficients for M⁺ and O⁺ ions. The molecular ions (M⁺) recombine with electrons directly and produce neutral atoms via a dissociative recombination process (Rishbeth & Garriott, 1969). The dissociative recombination process is much faster and responds almost instantly to the change in X-ray and EUV flux. In contrast, the photochemical loss of the O⁺ (and all its excited states) ions is primarily governed by two reactions, $O^+ + N_2 \rightarrow NO^+ + N$ and $O^+ + O_2 \rightarrow O_2^+ + O$, which are significantly slower (~ 1000 times slower (Rishbeth, 1970; Schunk & Nagy, 2009)) than the dissociative recombination process. Once NO⁺ and O₂⁺ are created by the above process they recombine with electrons via the dissociative recombination process. Therefore O⁺ and associated electrons at the F₂-layer heights have a longer lifetime. The N₂ density is much higher than that of O₂, which suggests that the first reaction dominates the formation and characteristics of the TSE-driven G-condition.

3.4 Effects of Geomagnetic Field Line Structure

Here we investigate whether magnetic latitude (field line orientation) affects the characteristics of the ionospheric G-condition. Figure 7(a) presents a contour plot of the eclipse shadow (occultation) over the CONUS, color-coded by the color bar on the right. The three magenta dots in the figure represent the locations of the peak of the eclipse shadow and $\pm 8^\circ$ latitudes from the peak. All three points are at the same longitude to remove any local time effect on the G-condition, which is beyond the scope of this study. Figures 7(b-d) present the modeled G-conditions at the peak of the eclipse shadow, at -8° , $+8^\circ$ latitude from the peak locations respectively. Note that, as per this WACCM-X simulation, not all the eclipse-shadowed regions observed a G-condition during the 2017 GAE. Occultation levels below 35% did not coincide with a G-condition, and we choose this latitude range $\pm 8^\circ$ from the center for this experiment. Quantifying factors of the G-condition, i.e., ΔT_{GC} and GCP , are mentioned in the panels. It is noteworthy that two locations away from the peak have similar eclipse shadows (α) and should observe similar G-conditions. Simulations predict higher GCP and longer ΔT_{GC} at the higher latitude ($+8^\circ$ latitude from the peak location), suggesting a stronger G-condition. The simulation presented here shows G-conditions are predominately observed at higher latitudes, which opposes characteristics of the G-condition mentioned in Rishbeth (1968). However, this simulation study is able to examine latitudinal effects within $\pm 8^\circ$ magnetic latitudes bounded within 55° magnetic latitude.

According to simulations, the G-condition occurs in areas with more than 75% obscuration and lasts for 40 minutes to an hour. To further demonstrate this we conducted a data-model comparison listed in Table 1. MHISR, located $\sim 9^\circ$ to the north from totality, observed a G-condition with $\Delta T_{GC}=54$ minutes and $GCP=288.8$ el/cc. The WACCM-X model simulation predicts a G-condition over MHISR lasting about 45 minutes with $GCP=135.1$ el/cc. It is also noteworthy that the F-peak at Millstone Hill (MA) appeared at ~ 160 kilometers which is 10 kilometers above the observed F-peak by the ionosondes located at Lusk (WY) and Boulder (CO). These results suggest that (i) the ionospheric G-condition might be affected by pre-eclipse background conditions, solar activity prior to this eclipse, and longitudinal/local time effects which are not incorporated in WACCM-X physics; (ii) the probability of the G-condition increases with an increase

in latitude. In the future, a comparative study of TSE-driven G-conditions in different magnetic geometries using observations and modeling is required to fully examine this hypothesis and comprehend the physics.

Place	Location [from Totality]	Local Time	ΔT_{GC} (min)[O/M] ^a	GC ^P (el/cc)[O/M] ^a
MHISR	$\sim 9^\circ\text{N}$	14	54/45	288.8/135.1
Lusk	$\sim 0^\circ\text{N}$	11	45/45	-/269.8
Boulder	$\sim 3.1^\circ\text{S}$	11	45/46	-/240.7

Table 1. Data-model comparison of the ionospheric G-condition observed at different latitudes and local time. ^a[O/M] refer to observation and model, respectively. Note that, GC^P can not be estimated for ionosonde observations, located at Lusk and Boulder.

4 Discussion

TSE conditions provide a remarkable opportunity to study the effects of a supersonic cooling shadow on the IT system. This study aims to develop a deeper understanding of TSE-driven effects on HF propagation and the ionospheric G-condition caused by changes in the IT system following the 2017 GAE. In this paper, we conducted a data-model comparison to understand the mechanism of the ionospheric G-condition following the 2017 GAE. In previous sections, we compared the observations against model simulations, conducted an analysis of the O^+ continuity equation, and studied the impact of magnetic field line structure on the G-condition. In this section, we discuss the perceived impact of the ionospheric G-condition in the context of the previous studies and the probable cause of latitudinal or local time modulation effects in the G-condition observed by various bottom-side ionospheric sounders.

During the 21 August 2017 GAE, ionosondes located at Lusk (WY) and Boulder (CO), and MHISR were located under the totality, 3°S , and 9°N of totality, respectively. All these bottom side sounders observed the ionospheric G-condition (Bullett & Mabie, 2018). Goncharenko et al. (2018) identified an anomalous condition which shows a low F-peak, below 200 kilometers, following the occultation peak at Millstone Hill. Additionally, the F-peak observed over MHISR occurred at 160-kilometer altitude, almost 10 kilometers higher than the G-condition observed near the eclipse totality. MHISR observed the largest change in electron density at F₂-layer heights (Goncharenko et al., 2018), in contrast to the results reported in previous simulation studies (Roble et al., 1986; Ding et al., 2010). The WACCM-X simulations confirm that eclipse-driven reduction in electron density affected all ionospheric layers (refer to Figure 3). Diagnostic analysis of O^+ showed that the observed ionospheric G-condition following the 2017 GAE is attributed to the slower recombination rates, due to the higher radiative lifetime of the O^+ ions (and associated electrons) at the F₂-layer altitudes (≥ 200 kilometers). Additionally, the analysis showed altitude variations of the O^+ recombination rate, which created a varying delay in peak electron density in response to eclipse shadow in the recovery phase. This variable delay with altitude is observed during the recovery phase, thus it creates an asymmetry in the ionospheric response in comparison with the period before the eclipse totality. These findings are also consistent with Wang et al. (2019). The degree of asymmetry observed in plasma density increases with altitude (refer to Figure 5). A study by Goncharenko et al. (2018), showed this asymmetrical behavior is not confined only to ionospheric plasma density, as it was also observed in ionospheric electron and ion temperatures, as well as vertical plasma velocity, which is not yet fully understood and will be the subject of future studies.

The upper ionosphere, primarily beyond 300 kilometers, is primarily controlled by transport processes, such as drift and diffusion (Schunk & Nagy, 2009). At higher latitudes, magnetic tilt angle plays a significant role in driving IT dynamics (Schlesier & Buonsanto, 1999; Schunk & Nagy, 2009). Plasma diffusion along the equipotential geomagnetic field lines can modulate the response of an ionospheric phenomenon, compared to the same phenomena observed at lower latitudes. In a study Rishbeth (1968) hypothesized that at higher latitudes plasma diffusion from the conjugate hemisphere along the field line fills the TSE-induced plasma vacancy at the F₂-layer altitude which reduces the occurrence probability of the ionospheric G-condition. A study by (Yau et al., 2018), showed a downward O⁺ ion flow with a speed of ~ 100 m/s, inside the eclipse shadow region, following the 2017 GAE. The modeling study conducted here showed that the strength of the TSE-driven ionospheric G-condition is highest at the totality. Additionally, the duration and strength of the G-condition observed at the higher latitude is higher than the same observed at the lower latitudes in the observations (refer to Table 1), and the WACCM-X model simulations (refer to Figure 7). The simulation study was done along one latitude, while observations listed in Table 1 were taken from instruments located in different latitudes or local times. Additionally, the conjugate hemispheres described in WACCM-X are not connected via magnetic field lines, so the simulation study presented here is not comprehensive enough to test the hypothesis described in Rishbeth (1968). A further data-model investigation is needed to confirm the hypothesis and to answer the probable cause of this latitudinal dependency of the ionospheric G-condition.

5 Summary & Conclusions

In this study, we present a physical formation mechanism of the ionospheric G-condition following the 2017 Great American Eclipse. We used Whole Atmosphere Community Climate Model with a Thermosphere and Ionosphere eXtension (WACCM-X) simulations to investigate the mechanism. Specifically, we conducted a diagnostic analysis of the atomic oxygen ion continuity equation. The following points summarize the findings of this simulation study that explain some ionospheric features observed during 2017 GAE:

- a) The ion density (and electron density) in the E-, F₁-, and F₂- layers all decrease in response to the eclipse, with the peak depletion and recovery in the E- and F₁- layers closely following the peak occultation and the recovery phase of the eclipse. However, the peak depletion in the F₂-layer is delayed almost 20 minutes at 240 kilometers, and this delay increases at higher altitudes. These simulation results are consistent with observations reported in previous studies (Goncharenko et al., 2018; Wang et al., 2019; Zhang et al., 2017).
- b) The delay creates an interval about 20 minutes after the peak occultation when the ion density in the F₁-layer is recovering while the density in the F₂-layer is still decreasing. This creates a situation where plasma density in the F₁-layer becomes greater than that in the F₂-layer for about 50 minutes, which manifests as the G-condition following the GAE, reported by Bullett and Mabie (2018). This result also suggests an anomalous F-peak condition, i.e., a low F₂-region peak reported by Goncharenko et al. (2018).
- c) Our study shows that the delayed photochemical recombination process associated with O⁺ ions in the F₂-layer is a primary mechanism responsible for creating the TSE-driven G-condition
- d) The data-model comparison study shows a stronger G-condition at higher latitudes, which is opposite to conclusions of Rishbeth (1968).

6 Open Research

All the data and simulation results are uploaded into the Zenodo repository and available for public use (Chakraborty, 2022). The majority of the analysis and visual-

ization were completed with the help of free, open-source software tools such as matplotlib (Hunter, 2007), IPython (Perez & Granger, 2007), pandas (McKinney, 2010), and others (Millman & Aivazis, 2011, e.g.). The code is published in the Zenodo repository (Chakraborty, 2022). The eclipse occultation mask has been computed with PyEclipse software freely available at Zenodo (Mrak, 2022).

Acknowledgments

SC thanks to the National Science Foundation (NSF) and the National Aeronautics and Space Administration for support under grants AGS-1935110 and 80NSSC20K1380, respectively. SM thanks to the National Science Foundation (NSF) and the Aeronautics and Space Administration for support under AGS-1929879 and 80NSSC22K0324, respectively. LQ is supported by NASA 80NSSC19K0278, 80NSSC20K0189, NNH19ZDA001N-HSR, and 80NSSC20K0018. PJE and LPG acknowledge research support at MIT Haystack Observatory through NSF grant AGS-1952737. The Millstone Hill Geospace Facility (including the Millstone Hill ISR) is operated for the community by the Massachusetts Institute of Technology under the same grant. This material is based upon work supported by the National Center for Atmospheric Research, which is a major facility sponsored by the NSF under Cooperative Agreement No. 1852977. Any opinions, findings, conclusions, or recommendations expressed in this material do not necessarily reflect the views of the NSF. The authors would also like to acknowledge the use of computational resources (<https://10.5065/D6RX99HX>) at the NCAR-Wyoming Supercomputing Center provided by the NSF and the State of Wyoming and supported by NCAR's Computational and Information Systems Laboratory for the WACCM-X simulations.

References

- Banks, P. M., Schunk, R. W., & Raitt, W. J. (1974). No+ and o+ in the high latitude f-region. *Geophysical Research Letters*, 1(6), 239-242. Retrieved from <https://agupubs.onlinelibrary.wiley.com/doi/abs/10.1029/GL001i006p00239> doi: <https://doi.org/10.1029/GL001i006p00239>
- Bullett, T., & Mabie, J. (2018). Vertical and oblique ionosphere sounding during the 21 august 2017 solar eclipse. *Geophysical Research Letters*, 45(8), 3690-3697. Retrieved from <https://agupubs.onlinelibrary.wiley.com/doi/abs/10.1002/2018GL077413> doi: <https://doi.org/10.1002/2018GL077413>
- Buonsanto, M. (1990). Observed and calculated f2 peak heights and derived meridional winds at mid-latitudes over a full solar cycle. *Journal of Atmospheric and Terrestrial Physics*, 52(3), 223-240. Retrieved from <https://www.sciencedirect.com/science/article/pii/0021916990901268> doi: [https://doi.org/10.1016/0021-9169\(90\)90126-8](https://doi.org/10.1016/0021-9169(90)90126-8)
- Chakraborty, S. (2022, August). *shibaji7/solareclipse: G-condition study v2.0*. Zenodo. Retrieved from <https://doi.org/10.5281/zenodo.6998026> doi: [10.5281/zenodo.6998026](https://doi.org/10.5281/zenodo.6998026)
- Chamberlin, P. C., Eparvier, F. G., Knoer, V., Leise, H., Pankratz, A., Snow, M., ... Woods, T. N. (2020). The flare irradiance spectral model-version 2 (fism2). *Space Weather*, 18(12), e2020SW002588. Retrieved from <https://agupubs.onlinelibrary.wiley.com/doi/abs/10.1029/2020SW002588> (e2020SW002588 10.1029/2020SW002588) doi: <https://doi.org/10.1029/2020SW002588>
- Chen, G., Wu, C., Huang, X., Zhao, Z., Zhong, D., Qi, H., ... Wang, J. (2015). Plasma flux and gravity waves in the midlatitude ionosphere during the solar eclipse of 20 may 2012. *Journal of Geophysical Research: Space Physics*, 120(4), 3009-3020. Retrieved from <https://agupubs.onlinelibrary.wiley.com/doi/abs/10.1002/2014JA020849> doi: <https://doi.org/10.1002/2014JA020849>

- Chen, G., Zhao, Z., Ning, B., Deng, Z., Yang, G., Zhou, C., ... Li, N. (2011). Latitudinal dependence of the ionospheric response to solar eclipse of 15 January 2010. *Journal of Geophysical Research: Space Physics*, 116(A6). Retrieved from <https://agupubs.onlinelibrary.wiley.com/doi/abs/10.1029/2010JA016305> doi: <https://doi.org/10.1029/2010JA016305>
- Cnossen, I., Ridley, A. J., Goncharenko, L. P., & Harding, B. J. (2019). The response of the ionosphere-thermosphere system to the 21 August 2017 solar eclipse. *Journal of Geophysical Research: Space Physics*, 124(8), 7341-7355. Retrieved from <https://agupubs.onlinelibrary.wiley.com/doi/abs/10.1029/2018JA026402> doi: <https://doi.org/10.1029/2018JA026402>
- Cummack, C. H. (1961). Evidence of some geomagnetic control on the F1-layer. *Journal of Atmospheric and Terrestrial Physics*, 22(2), 157-158. doi: 10.1016/0021-9169(61)90151-9
- Deminov, M. G., Romanova, E. B., & Tashchilin, A. V. (2011, Sep 29). Origination of g conditions in the ionospheric f region depending on solar and geomagnetic activity. *Geomagnetism and Aeronomy*, 51(5), 669. Retrieved from <https://doi.org/10.1134/S0016793211050045> doi: 10.1134/S0016793211050045
- Ding, F., Wan, W., Ning, B., Liu, L., Le, H., Xu, G., ... Yang, M. (2010). Gps tec response to the 22 July 2009 total solar eclipse in east Asia. *Journal of Geophysical Research: Space Physics*, 115(A7). Retrieved from <https://agupubs.onlinelibrary.wiley.com/doi/abs/10.1029/2009JA015113> doi: <https://doi.org/10.1029/2009JA015113>
- Fukao, S., Oliver, W., Onishi, Y., Takami, T., Sato, T., Tsuda, T., ... Kato, S. (1991). F-region seasonal behavior as measured by the mu radar. *Journal of Atmospheric and Terrestrial Physics*, 53(6), 599-618. Retrieved from <https://www.sciencedirect.com/science/article/pii/0021916991900880> (The Symposium on Thermospheric and Ionospheric Dynamics) doi: [https://doi.org/10.1016/0021-9169\(91\)90088-O](https://doi.org/10.1016/0021-9169(91)90088-O)
- Goncharenko, L. P., Erickson, P. J., Zhang, S.-R., Galkin, I., Coster, A. J., & Jonah, O. F. (2018). Ionospheric response to the solar eclipse of 21 August 2017 in millstone hill (42n) observations. *Geophysical Research Letters*, 45(10), 4601-4609. Retrieved from <https://agupubs.onlinelibrary.wiley.com/doi/abs/10.1029/2018GL077334> doi: 10.1029/2018GL077334
- Hairston, M. R., Mrak, S., Coley, W. R., Burrell, A., Holt, B., Perdue, M., ... Power, R. (2018). Topside ionospheric electron temperature observations of the 21 August 2017 eclipse by dmsp spacecraft. *Geophysical Research Letters*, 45(15), 7242-7247. Retrieved from <https://agupubs.onlinelibrary.wiley.com/doi/abs/10.1029/2018GL077381> doi: <https://doi.org/10.1029/2018GL077381>
- Harding, B. J., Drob, D. P., Buriti, R. A., & Makela, J. J. (2018). Nightside detection of a large-scale thermospheric wave generated by a solar eclipse. *Geophysical Research Letters*, 45(8), 3366-3373. Retrieved from <https://agupubs.onlinelibrary.wiley.com/doi/abs/10.1002/2018GL077015> doi: <https://doi.org/10.1002/2018GL077015>
- Heelis, R. A., Lowell, J. K., & Spiro, R. W. (1982). A model of the high-latitude ionospheric convection pattern. *Journal of Geophysical Research: Space Physics*, 87(A8), 6339-6345. Retrieved from <https://agupubs.onlinelibrary.wiley.com/doi/abs/10.1029/JA087iA08p06339> doi: <https://doi.org/10.1029/JA087iA08p06339>
- Hunter, J. D. (2007). Matplotlib: A 2D graphics environment. *Computing In Science & Engineering*, 9(3), 90-95. Retrieved from <https://ieeexplore.ieee.org/document/4160265> doi: 10.1109/MCSE.2007.55
- Häggström, I., & Collis, P. (1990). Ion composition changes during f-region density depletions in the presence of electric fields at auroral latitudes.

- Journal of Atmospheric and Terrestrial Physics*, 52(6), 519-529. Retrieved from <https://www.sciencedirect.com/science/article/pii/S002191699090050W> (The Fourth International EISCAT Workshop) doi: [https://doi.org/10.1016/0021-9169\(90\)90050-W](https://doi.org/10.1016/0021-9169(90)90050-W)
- Lei, J., Wang, W., Burns, A. G., Solomon, S. C., Richmond, A. D., Wiltberger, M., ... Reinisch, B. W. (2008). Observations and simulations of the ionospheric and thermospheric response to the december 2006 geomagnetic storm: Initial phase. *Journal of Geophysical Research: Space Physics*, 113(A1). Retrieved from <https://agupubs.onlinelibrary.wiley.com/doi/abs/10.1029/2007JA012807> doi: <https://doi.org/10.1029/2007JA012807>
- Liu, H.-L., Bardeen, C. G., Foster, B. T., Lauritzen, P., Liu, J., Lu, G., ... Wang, W. (2018). Development and validation of the whole atmosphere community climate model with thermosphere and ionosphere extension (waccm-x 2.0). *Journal of Advances in Modeling Earth Systems*, 10(2), 381-402. Retrieved from <https://agupubs.onlinelibrary.wiley.com/doi/abs/10.1002/2017MS001232> doi: <https://doi.org/10.1002/2017MS001232>
- Liu, H.-L., Foster, B. T., Hagan, M. E., McInerney, J. M., Maute, A., Qian, L., ... Oberheide, J. (2010). Thermosphere extension of the whole atmosphere community climate model. *Journal of Geophysical Research: Space Physics*, 115(A12). Retrieved from <https://agupubs.onlinelibrary.wiley.com/doi/abs/10.1029/2010JA015586> doi: <https://doi.org/10.1029/2010JA015586>
- Lobzin, V. V., & Pavlov, A. V. (2002). G condition in the f2 region peak electron density: a statistical study. *Annales Geophysicae*, 20(4), 523-537. Retrieved from <https://angeo.copernicus.org/articles/20/523/2002/> doi: [10.5194/angeo-20-523-2002](https://doi.org/10.5194/angeo-20-523-2002)
- McInerney, J. M., Marsh, D. R., Liu, H.-L., Solomon, S. C., Conley, A. J., & Drob, D. P. (2018). Simulation of the 21 august 2017 solar eclipse using the whole atmosphere community climate model-extended. *Geophysical Research Letters*, 45(9), 3793-3800. Retrieved from <https://agupubs.onlinelibrary.wiley.com/doi/abs/10.1029/2018GL077723> doi: <https://doi.org/10.1029/2018GL077723>
- McKinney, W. (2010). Data Structures for Statistical Computing in Python. In S. van der Walt & J. Millman (Eds.), *Proceedings of the 9th python in science conference* (pp. 56-61). Retrieved from <https://conference.scipy.org/proceedings/scipy2010/mckinney.html> doi: 10.25080/Majora-92bf1922-012
- Millman, K. J., & Aivazis, M. (2011). Python for Scientists and Engineers. *Computing in Science & Engineering*, 13(2), 9-12. Retrieved from <https://ieeexplore.ieee.org/document/5725235> doi: 10.1109/MCSE.2011.36
- Mrak, S. (2022, September). *aldebaran1/pyeclipse: v0.1.0*. Zenodo. Retrieved from <https://doi.org/10.5281/zenodo.7044996> doi: 10.5281/zenodo.7044996
- Mrak, S., Semeter, J., Drob, D., & Huba, J. D. (2018). Direct euv/x-ray modulation of the ionosphere during the august 2017 total solar eclipse. *Geophysical Research Letters*, 45(9), 3820-3828. Retrieved from <https://agupubs.onlinelibrary.wiley.com/doi/abs/10.1029/2017GL076771> doi: <https://doi.org/10.1029/2017GL076771>
- Mrak, S., Zhu, Q., Deng, Y., Dammasch, I. E., Dominique, M., Hairston, M. R., ... Semeter, J. (2022). Modeling solar eclipses at extreme ultra violet wavelengths and the effects of nonuniform eclipse shadow on the ionosphere-thermosphere system. *Journal of Geophysical Research: Space Physics*, 127(12), e2022JA031058. Retrieved from <https://agupubs.onlinelibrary.wiley.com/doi/abs/10.1029/2022JA031058> (e2022JA031058 2022JA031058) doi: <https://doi.org/10.1029/2022JA031058>
- Oliver, W. L. (1990). Neutral and ion composition changes in the f region over millstone hill during the equinox transition study. *Journal of Geophysical Re-*

- search: *Space Physics*, 95(A4), 4129-4134. Retrieved from <https://agupubs.onlinelibrary.wiley.com/doi/abs/10.1029/JA095iA04p04129> doi: <https://doi.org/10.1029/JA095iA04p04129>
- Pavlov, A., Buonsanto, M., Schlesier, A., & Richards, P. (1999). Comparison of models and data at millstone hill during the 5–11 june 1991 storm. *Journal of Atmospheric and Solar-Terrestrial Physics*, 61(3), 263-279. Retrieved from <https://www.sciencedirect.com/science/article/pii/S1364682698001357> doi: [https://doi.org/10.1016/S1364-6826\(98\)00135-7](https://doi.org/10.1016/S1364-6826(98)00135-7)
- Pavlov, A. V., & Buonsanto, M. J. (1998, Apr 01). Anomalous electron density events in the quiet summer ionosphere at solar minimum over millstone hill. *Annales Geophysicae*, 16(4), 460-469. Retrieved from <https://doi.org/10.1007/s00585-998-0460-8> doi: 10.1007/s00585-998-0460-8
- Perez, F., & Granger, B. E. (2007, May). Ipython: A system for interactive scientific computing. *Computing in Science Engineering*, 9(3), 21-29. Retrieved from <https://ieeexplore.ieee.org/document/4160251> doi: 10.1109/MCSE.2007.53
- Richards, P. G., & Voglozin, D. (2011). Reexamination of ionospheric photochemistry. *Journal of Geophysical Research: Space Physics*, 116(A8). Retrieved from <https://agupubs.onlinelibrary.wiley.com/doi/abs/10.1029/2011JA016613> doi: <https://doi.org/10.1029/2011JA016613>
- Richmond, A. (1992). Assimilative mapping of ionospheric electrodynamics. *Advances in Space Research*, 12(6), 59-68. Retrieved from <https://www.sciencedirect.com/science/article/pii/0273117792900405> doi: [https://doi.org/10.1016/0273-1177\(92\)90040-5](https://doi.org/10.1016/0273-1177(92)90040-5)
- Richmond, A., Lu, G., Emery, B., & Knipp, D. (1998). The amie procedure: Prospects for space weather specification and prediction. *Advances in Space Research*, 22(1), 103-112. Retrieved from <https://www.sciencedirect.com/science/article/pii/S0273117797011083> (Solar-Terrestrial Relations: Predicting the Effects on the Near-Earth Environment) doi: [https://doi.org/10.1016/S0273-1177\(97\)01108-3](https://doi.org/10.1016/S0273-1177(97)01108-3)
- Rishbeth, H. (1968, sep). Solar eclipses and ionospheric theory. , 8(4), 543–554.
- Rishbeth, H. (1970). Eclipse effects in the ionosphere. *Nature*, 226(5251), 1099–1100. doi: 10.1038/2261099A0
- Rishbeth, H., & Garriott, O. K. (1969). *Introduction to ionospheric physics*. Academic Press, New York.
- Roble, R. G., Emery, B. A., & Ridley, E. C. (1986). Ionospheric and thermospheric response over millstone hill to the may 30, 1984, annular solar eclipse. *Journal of Geophysical Research: Space Physics*, 91(A2), 1661-1670. Retrieved from <https://agupubs.onlinelibrary.wiley.com/doi/abs/10.1029/JA091iA02p01661> doi: <https://doi.org/10.1029/JA091iA02p01661>
- Schlesier, A. C., & Buonsanto, M. J. (1999). Observations and modeling of the april 10–12, 1997 ionospheric storm at millstone hill. *Geophysical Research Letters*, 26(15), 2359-2362. Retrieved from <https://agupubs.onlinelibrary.wiley.com/doi/abs/10.1029/1999GL900486> doi: <https://doi.org/10.1029/1999GL900486>
- Schunk, R., & Nagy, A. (2009). *Ionospheres: Physics, Plasma Physics, and Chemistry* (2nd ed.). Cambridge University Press. doi: 10.1017/CBO9780511635342
- Solomon, S. C., & Qian, L. (2005). Solar extreme-ultraviolet irradiance for general circulation models. *Journal of Geophysical Research: Space Physics*, 110(A10). Retrieved from <https://agupubs.onlinelibrary.wiley.com/doi/abs/10.1029/2005JA011160> doi: <https://doi.org/10.1029/2005JA011160>
- Tsai, H. F., & Liu, J. Y. (1999). Ionospheric total electron content response to solar eclipses. *Journal of Geophysical Research: Space Physics*, 104(A6), 12657-12668. Retrieved from <https://agupubs.onlinelibrary.wiley.com/doi/>

- abs/10.1029/1999JA900001 doi: <https://doi.org/10.1029/1999JA900001>
- Wang, W., Dang, T., Lei, J., Zhang, S., Zhang, B., & Burns, A. (2019). Physical processes driving the response of the f2 region ionosphere to the 21 august 2017 solar eclipse at millstone hill. *Journal of Geophysical Research: Space Physics*, 124(4), 2978-2991. Retrieved from <https://agupubs.onlinelibrary.wiley.com/doi/abs/10.1029/2018JA025479> doi: <https://doi.org/10.1029/2018JA025479>
- Weimer, D. R. (2005). Improved ionospheric electrodynamic models and application to calculating joule heating rates. *Journal of Geophysical Research: Space Physics*, 110(A5). Retrieved from <https://agupubs.onlinelibrary.wiley.com/doi/abs/10.1029/2004JA010884> doi: <https://doi.org/10.1029/2004JA010884>
- Yau, A. W., Foss, V., Howarth, A. D., Perry, G. W., Watson, C., & Huba, J. (2018). Eclipse-induced changes to topside ion composition and field-aligned ion flows in the august 2017 solar eclipse: e-pop observations. *Geophysical Research Letters*, 45(20), 10,829-10,837. Retrieved from <https://agupubs.onlinelibrary.wiley.com/doi/abs/10.1029/2018GL079269> doi: <https://doi.org/10.1029/2018GL079269>
- Zhang, S.-R., Erickson, P. J., Goncharenko, L. P., Coster, A. J., Rideout, W., & Vierinen, J. (2017). Ionospheric bow waves and perturbations induced by the 21 august 2017 solar eclipse. *Geophysical Research Letters*, 44(24), 12,067-12,073. Retrieved from <https://agupubs.onlinelibrary.wiley.com/doi/abs/10.1002/2017GL076054> doi: <https://doi.org/10.1002/2017GL076054>

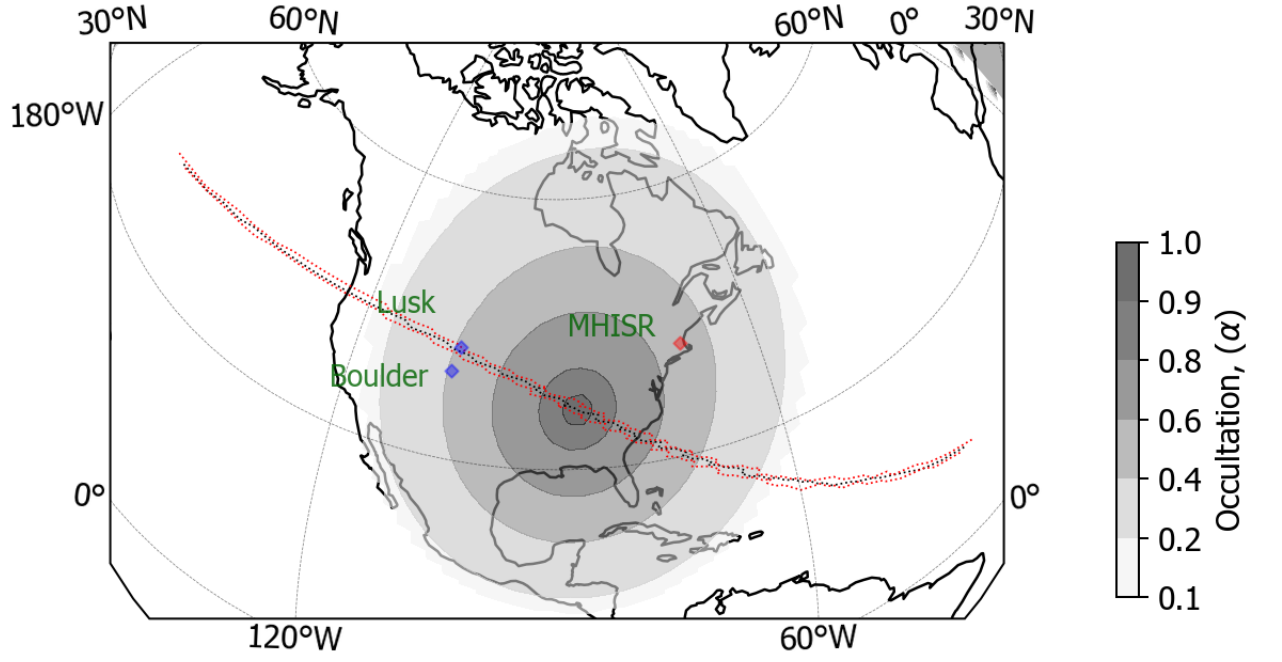


Figure 1. Locations of the instruments used in the study. Eclipse obscuration shadow is overlaid in gray and color coded by color bar on right during the peak of totality. Red and black dashed curves indicate the location of eclipse totality across the TSE passage. Ionosondes and MHISR are color coded by blue and red diamonds, respectively.

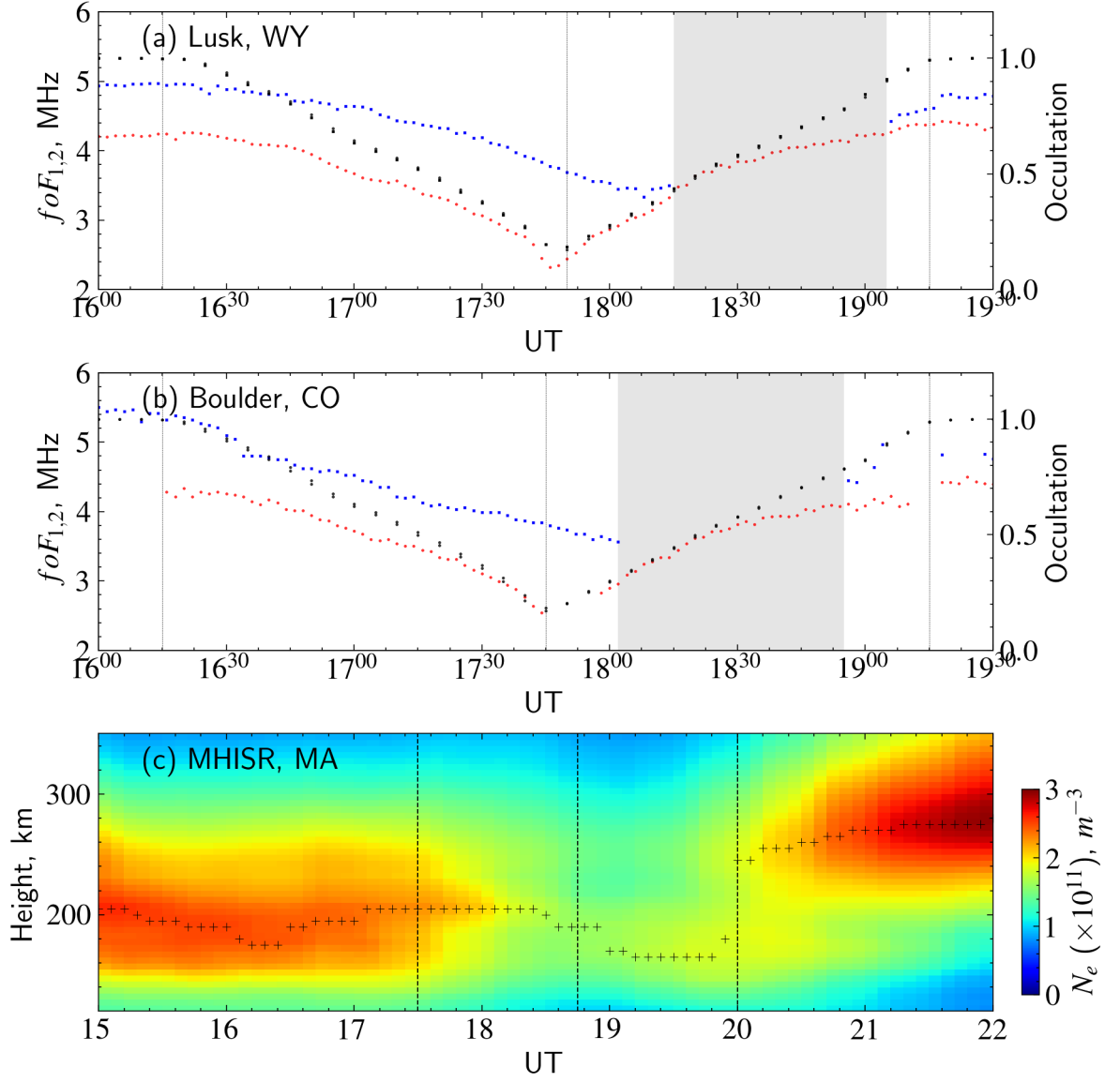


Figure 2. Timeseries of plasma frequency and electron density observed using ionosonde, ISR Millstone Hill: (a) $foF_{1,2}$ and eclipse occultation functions (in black) at 150 and 240 kilometers altitudes over Lusk (WY), (b) $foF_{1,2}$ and eclipse occultation functions (in black) at 150 and 240 kilometers altitudes over Boulder (CO), (c) electron density at Millstone Hill (MA), respectively. Black circle and squares represent eclipse occultation functions at 150 and 240 kilometer altitudes, respectively. Vertical black lines in panels represent the start, minimum, and end of the eclipse at corresponding locations, respectively.

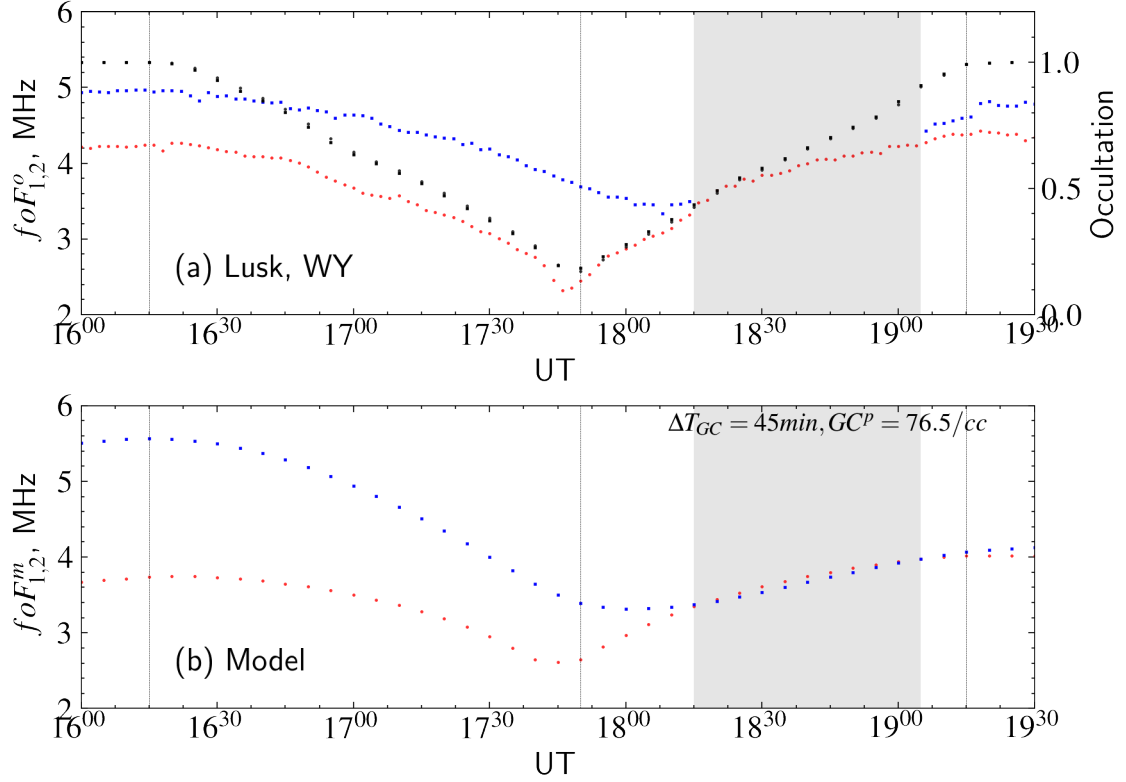


Figure 3. Data-model (WACCM-X simulation) comparison of the ionospheric G-condition during 2017 GAE: (a) $foF_{1,2}^o$ observation from ionosonde located at Lusk (WY) and (b) modeled $foF_{1,2}^m$ simulated using WACCM-X model over Lusk (WY). Vertical black lines in panels represent the start, minimum, and end of the partial eclipse over Lusk (WY), respectively. The gray shadow identifies the time window when $foF_1 \geq foF_2$, the ionospheric G-condition, observed by the ionosonde and the model. Black circle and squares represent eclipse occultation functions at 150 and 240 kilometer altitudes, respectively.

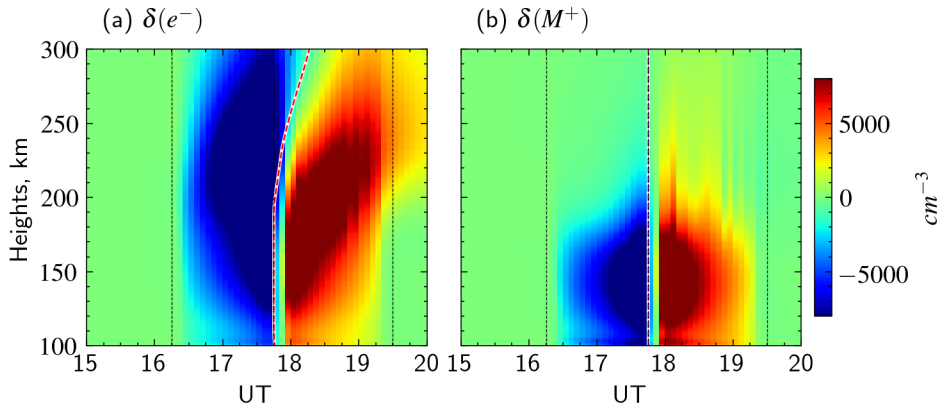


Figure 4. 2D Time-altitude distributions of differential-difference of the (a) electron and (b) M^+ ion densities over Lusk (WY). The vertical magenta curve in each panel identifies the time when parameters reach minimum value, as a function of altitude. The vertical dashed lines show the time of start, maximum obscuration, and end of the eclipse at Lusk (WY).

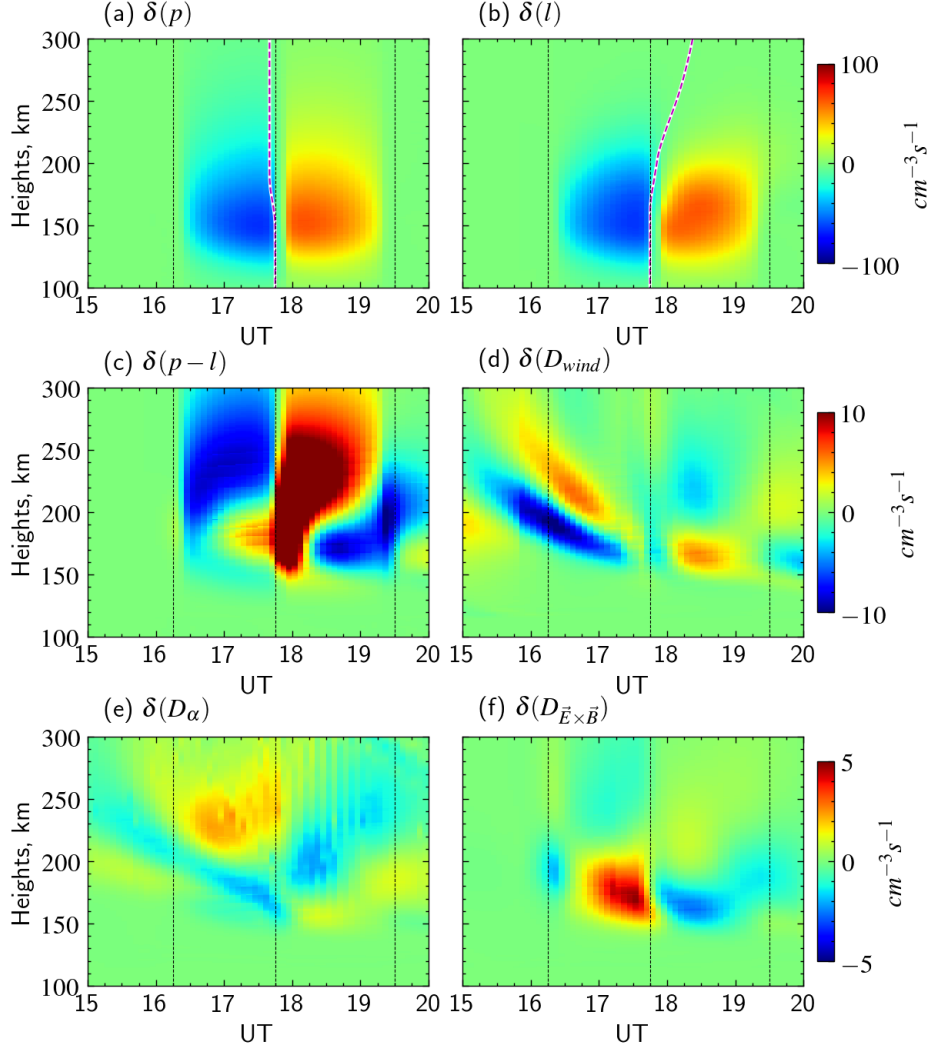


Figure 5. 2D Time-altitude distributions of differential-difference of the diagnostic analysis of O^+ ions: (a) chemical production, (b) chemical loss, (c) chemical production-loss, (d) transport due to neutral wind, (e) ambipolar diffusion, and (f) transport due to $\vec{E} \times \vec{B}$ drift over Lusk (WY). The vertical magenta curve in panels identifies the time when parameters reach minimum value, as a function of altitude. The vertical dashed lines show the time of start, maximum obscuration, and end of the eclipse at Lusk (WY).

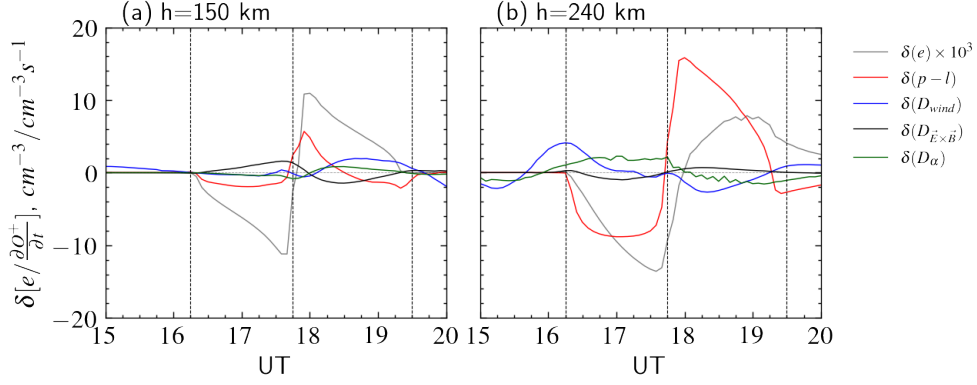


Figure 6. 1D time series of differential-difference of the electron density and diagnostic analysis (in gray) of O^+ ions' chemical production-loss (in red), transport due to neutral wind (in blue), ambipolar diffusion (in black), and transport due to $\vec{E} \times \vec{B}$ drift (in green) at (a) 150 kilometers and (b) 240 kilometers over Lusk (WY). The vertical dashed lines show the time of start, maximum obscuration, and end of the eclipse at Lusk (WY).

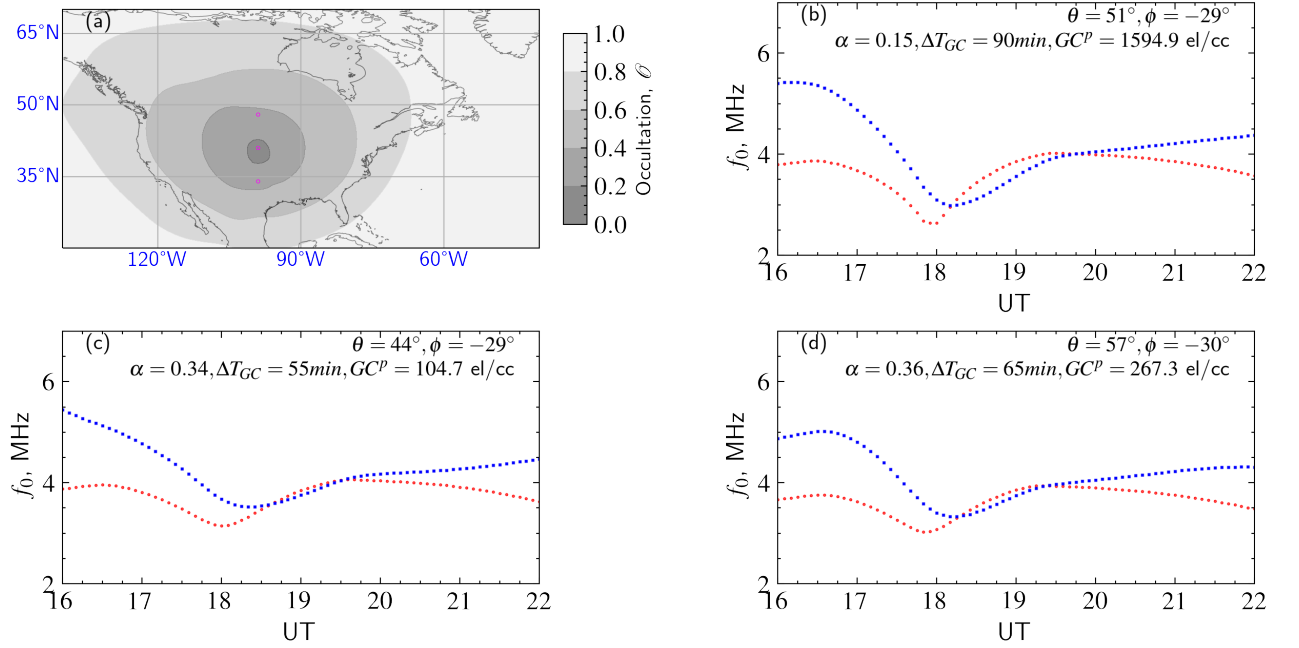


Figure 7. (a) Shadow of solar eclipse over North American sector in geographic coordinates, the magenta circles indicate three locations, peak of the eclipse shadow, and $\pm 8^\circ$ latitudes from the center; (b) modeled G-condition at the peak of the eclipse shadow; (c) modeled G-condition at -8° latitude from the peak of the eclipse shadow; and (d) modeled G-condition at $+8^\circ$ latitude from the peak of the eclipse shadow. Geomagnetic coordinates of each location, occultation (α), ΔT_{GC} , and GC^P is mentioned in panels (b-d).